Electronic Structure and Charge Transfer in the TiO$_2$ Rutile (110)/Graphene Composite Using Hybrid DFT Calculations

Peter Gillespie* and Natalia Martsinovich*

Department of Chemistry, University of Sheffield, Brook Hill, Sheffield, UK, S3 7HF

E-mail: pnogillespie1@sheffield.ac.uk; n.martsinovich@sheffield.ac.uk

1

Abstract

Composite systems of TiO_2 with nanocarbon materials, such as graphene, graphene oxide and carbon nanotubes, have proven to be efficient photocatalyst materials. However, detailed understanding of their electronic structure and the mechanisms of the charge transfer processes is still lacking. Here, we use hybrid density functional theory calculations to analyse the electronic properties of the ideal rutile (110)-graphene interface, in order to understand experimentally observed trends in photoinduced charge transfer. We show that the potential energy surface of pristine graphene physisorbed above rutile (110) is relatively flat, enabling many possible positions of graphene above the rutile (110) surface. We verify that tensile and compressive strain has negligible effect on the electronic properties of graphene at low levels of strain. By analysing the band structure of this composite material and the composition of the valence and conduction band edges, we show that both the highest occupied states and the lowest unoccupied states of this composite are dominated by graphene, and that there is also a significant contribution of Ti orbitals to the two lowest unoccupied bands. We suggest that a transition from graphene-dominated occupied bands to mixed graphene and TiO_2-based unoccupied bands is responsible for the experimentally observed photoinduced charge transfer from graphene to TiO_2 under visible light irradiation; however, the most stable state for an excess (e.g. photoexcited) electron is localised on the carbon orbitals, which make up the lowest-energy conduction band. This separation of photogenerated electrons and holes makes TiO_2-graphene an efficient photocatalyst material.

Introduction

Heterogeneous photocatalysis is a subject area which has seen continuous progress over the years[1–6] since the first proof-of-concept experiment by Fujishima and Honda.[7] The potential for such materials to be used for solar energy conversion, through photocatalytic water splitting or CO_2 reduction, is of tremendous importance for supplementing (and subsequently

reducing) the use of limited chemical fuel sources such as oil and natural gas. Furthermore, the ability for these functional materials to clean air and water borne pollutants from industrial sources should not be overlooked as these present a further environmental concern.[2,8–12]

Titanium dioxide (TiO_2) has been a popular material for heterogeneous photocatalysts in many forms due to its low cost, favourable band positions for water splitting, chemical stability, and versatility towards different forms of modification.[1,13–16] It is abundantly clear, however, that single-component photocatalysts are insufficient for solar energy applications, as metal oxides generally suffer from poor photocatalytic performance under solar irradiation — emanating from a wide band gap (3.0–3.2 eV for TiO_2) and high charge carrier recombination rates.[1–6,14,15]

Combination of TiO_2 with another semiconducting material in a heterojunction arrangement has been a long-studied concept in both photovoltaics and photocatalysis,[3,15,17,18] and has been quite successful as a means of tackling both the charge recombination problem (through interfacial charge carrier separation) and, by using a narrow-gap semiconductor, enabled extending photon absorption into the visible region. A popular approach from previous decades has been to combine TiO_2 with cadmium sulphide (CdS) quantum dots.[1,15] Anchoring CdS to the surface of TiO_2 has been shown to increase photocatalytic activity notably and longevity to some extent, however issues with photocorrosion in particular pose a problem for potential industrial applications.[6,14,19]

More recently, studies have been focussed on carbon-nanostructure/TiO_2 composite materials,[16,17,20,21] starting with carbon nanotubes (NTs)[22–27] following their isolation in the early 1990s.[28] Following a novel synthesis technique by Williams *et al*,[29] there has been a surge in interest in composites of TiO_2 with graphene.[13,30,31] Originally it was proposed that the large surface areas and electrical conductivities of these carbon nanostructures should help efficiently separate generated charge carriers, thus enhancing photocatalytic efficiency.[16,20] Numerous experimental studies[22,24,30,32–37] have demonstrated that the addition of graphene and carbon nanotubes to TiO_2 also extends the photon absorption spectrum of

the material into the visible region.

Such studies provide evidence for strong electronic interaction between the two systems, however, despite attempts to study the mechanism[31,38,39] the nature of this charge transfer across the interface is still not fully understood. In particular, the early experiments demonstrated that photoinduced electrons are transferred from TiO_2 to graphene,[29] so that graphene is expected to behave as an electron shuttle.[40] Shortly thereafter, photocurrent measurements together with theoretical calculations showed that enhanced light absorption originates from charge-transfer excitation from graphene to TiO_2, in the direction opposite to what previously observed.[41] Moreover, several experimental studies showed that charge transfer in both directions is possible (see the overview in Table 1), in particular, dependence of charge transfer direction on the excitation wavelength was demonstrated: from TiO_2 to graphene when excited by UV light, and from graphene to TiO_2 when excited by visible light.[38,39]

Computational studies of TiO_2-nanocarbon interfaces have made significant steps in understanding the nature of charge transfer. Notably, it has been demonstrated that there is strong electronic overlap and large interfacial binding energy across the physisorbed TiO_2 rutile (110)-graphene interface.[41] Ground-state charge transfer from graphene to TiO_2 has been demonstrated, as well as photoinduced charge transfer from graphene to TiO_2.[41] Time-dependent density functional theory (TD-DFT) and non-adiabatic molecular dynamics (NAMD) studies by Long and Prezhdo,[43] in addition to transient UV/Vis absorption spectroscopy measurements by Manga *et al*,[42] have shown that transfer of photoexcited electron from graphene to TiO_2 is efficient and is faster than the average excited state lifetime for graphene — with measured electron transfer timescales of 200–250 femtoseconds.[42] These studies have shown that graphene can act in this composite system as a visible/near infrared photon absorber (photosensitiser) and as a means of providing charge carrier separation, while the direction of charge transfer depends on the relative positions of electronic bands on each side of the interface.

Table 1: Overview of several experimental and computational investigations of photoinduced charge transfer in TiO$_2$-graphene systems

Research Article	System Studied	Methodology	Observed Direction of Charge Transfer
Experimental			
Manga et al. **2009**[42]	TiO$_2$/Graphene Oxide	Femtosecond transient UV absorption spectroscopy	Graphene to TiO$_2$
Liang et al. **2012**[39]	TiO$_2$/Graphene	UV-Visible photoluminescence quenching	Both directions possible
Pastrana-Martínez et al. **2012**[38]	TiO$_2$/Reduced Graphene Oxide	UV-Visible photocatalysis kinetics	Graphene to TiO$_2$ (Visible Light); TiO$_2$ to Graphene (UV Light)
Xu and Yang **2013**[31]	ZnO/Reduced Graphene Oxide	Visible-region photocatalysis kinetics	Graphene to ZnO
Theoretical			
Du et al. **2011**[41]	Rutile (110)/Graphene	LDA + U, electron/hole density plots, simulation of optical absorption	Graphene to Rutile
Long et al. **2012**[43]	Rutile (110)/Graphene	PBE + U, time-dependent DFT, non-adiabatic molecular dynamics	Graphene to Rutile
Li et al. **2013**[44]	Anatase (101)/Graphene	PBE + U, electron density difference, density of states	Graphene to Anatase
Masuda et al. **2014**[45]	Anatase (001)/Graphene	PBE + U, Bader charge analysis, electron density plots	Graphene to Anatase

These key studies were followed by a number of further studies of the interfaces of graphene with rutile[46] and anatase[44,45,47–50] polymorphs of TiO$_2$ and other oxides, such as CeO$_2$[51] and SrTiO$_3$,[52] as well as several studies of small TiO$_2$ clusters on graphene[53–58] and graphene-like flakes on TiO$_2$ surfaces,[59,60] and larger TiO$_2$/graphene/dye heterostructures.[61] Notably, several of these works confirm the role of graphene as photosensitiser, leading to photoinduced charge transfer from graphene to TiO$_2$,[44,50] similar to the first computational studies[41,43] and in agreement with experiments.[31,38,62] However, no computational studies have investigated the alternative process, photoinduced charge transfer from TiO$_2$ to graphene. This work aims to investigate the origins of the two experimentally observed directions of photoinduced charge transfer.

Studying the interface itself is, from a purely computational perspective, very challenging. First, the crystal structures of TiO_2 and graphene differ in size and shape. To generate the composite unit cell (UC), each component system needs to be extended such that the resulting composite supercells are commensurate. The resulting composite unit cells are typically very large (in the range of 100-300 atoms) and computationally demanding to simulate and require efficiently-scaling parallel software. Second, known shortcomings with pure DFT functionals are the underestimation of semiconductor band gaps[63] and the tendency to inaccurately delocalise the electron density.[64] To better represent the electronic properties of TiO_2, hybrid DFT/Hartree-Fock(HF) functionals can be used in the simulations, but with large systems such as those represented here the computational cost (typically depending on the number of basis functions n as n^4) is high. Finally, the system also contains semi-metallic graphene, which can make hybrid DFT simulations more susceptible to problems with numerical stability and requires careful selection of convergence parameters in the calculations (see the Computational Methodology section).

The complexity and the high computational expense of studying this interface practically limit the choice of the methods available for use. In particular, for this system it has been common for studies to employ pure DFT with a Hubbard 'U' correction,[65] which can correctly reproduce the band gaps and band positions of TiO_2, but where the choice of the parameter U can be quite ambiguous (values ranging from 4.0 to 5.5 eV[41,43,45,46,56,60] and even as high as 9.0 eV[44,48] have been used in studies of TiO_2-graphene interfaces). Hybrid functionals would be a more reliable choice,[66–68] which allow consistent comparison of TiO_2-based systems. However, to the best of our knowledge, only one group recently used hybrid DFT functionals to study a TiO_2 anatase (101)/graphene interface.[50,69] Even higher accuracy in describing the electronic structure of this system could, in principle, be achieved using many-body perturbation theory (such as the GW approximation used *e.g.* for bulk TiO_2 in Ref.[63]), but such calculations would be prohibitively expensive.

The aim of this study is to investigate the nature of a model rutile (110)/graphene inter-

face using high-accuracy hybrid DFT calculations, in particular focussing on the electronic structure and the nature of electron transfer in this system. To do this, we choose a range-separated screened-exchange HSE06 functional,[70,71] which gives accurate values of band gaps and defect states in TiO2 and other transition metal oxides.[66,72] To mitigate the difficulty of optimisation of large composite cells, we use a two-step procedure and perform optimisation using very efficient CP2K software[73] at the Γ **k**-point, followed by high-accuracy calculations of the electronic structure at a dense **k**-point grid using CRYSTAL14 software.[74] The manuscript is organised as follows. After outlining the computational methods used, we discuss the construction of the composite rutile (110)-graphene cell. Then, we explore the effect of strain (arising from lattice mismatch) on the electronic properties of graphene. After that, we explore the structure and interaction of the rutile (110)-graphene interface, followed by the analysis of the electronic structure of this interface. Finally, these properties are summarised and the charge transfer capabilities are discussed in the context of this work and the wider literature.

Computational Methodology

Computational Methods

All geometry optimisations and binding energy analyses were carried out using the QUICK-STEP program,[73] within the CP2K sofware package. All pure DFT calculations used the PBE[75] exchange-correlation functional, with empirical Grimme D2[76] dispersion correction included. The calculations utilised Goedecker-Teter-Hutter pseudopotentials[77] and double-zeta basis sets with diffuse and polarisation functions, which have been optimised for use in CP2K.[78] The vacuum space between graphene and the bottom of the periodic image of the TiO_2 slab was 19.5 Å. All atom positions were fully relaxed, similar to the previous studies of TiO_2[79–82] and TiO_2/graphene interfaces.[45–47] An alternative would be to fix the lowest layer of TiO_2 and saturate the dangling bonds with pseudo-hydrogen atoms, as done

e.g. in Ref.,[83] to avoid changes in the electronic structure due to fixed undercoordinated atoms. Basis set superposition error (BSSE) in calculations of binding energies was corrected using the counterpoise method.[84] For all hybrid DFT calculations the HSE06[70,71] range-separated exchange-correlation functional was used, in addition to the Auxiliary Density Matrix Method (ADMM),[85] featured in the CP2K software package. In such calculations Hartree-Fock exchange is computed with a much smaller auxiliary basis set, while the primary basis set (carried over from PBE-level calculations in this instance) is used in the non-HF exchange part of the functional. The auxiliary basis set cpFIT3 (contracted, 3 gaussian exponents per valence orbital, includes polarisation d-functions) was used for carbon and oxygen, while FIT11 (4 s, 3 p, and 3 d shells and 1 f shell in total) was used for titanium. An example of the input file with the settings used in this study is provided in the Supporting Information (SI).

The optimised coordinates obtained in CP2K HSE06 calculations were then used as input for calculations with a fine $\mathbf{k}$-point grid using the CRYSTAL14 software package.[74] All density of states, band structure, and graphene strain test calculations were carried out using CRYSTAL14. For calculations of properties of the rutile (110)/graphene interface a Monkhorst-Pack $\mathbf{k}$-point mesh of $12 \times 12 \times 1$ was used. For the graphene strain tests a denser $\mathbf{k}$-point mesh of $16 \times 16 \times 1$ was used. Band structures of graphene were calculated with 1800 points along the path, and band structures of the TiO_2/graphene composite with 300 points along the path. The DFT functional used for graphene strain tests was PBE (in line with the recent computational studies of graphene[86–89]), and the hybrid DFT functional used for TiO_2-graphene calculations was HSE06. Empirical Grimme D2 dispersion corrections were added in all CRYSTAL14 calculations. All these calculations used all-electron triple-zeta basis sets with polarisation functions from the work of M. Peintinger et $al.$[90] The height of the cell was formally set to 500 Å (no periodicity in the z direction in the 2D slab model in CRYSTAL). In order to obtain band energies relative to the vacuum level, the electrostatic potential of the vacuum region above the unit cell was calculated and was then subtracted

from each band energy.

Unit Cell Construction

To construct the unit cell of the rutile (110)/graphene composite, the lowest common multiples of the cell parameters of rutile (110) compared to graphene need to be found. The rutile (110) unit cell has a rectangular shape (see Figure 1), with cell parameters $A = 6.529$ Å and $B = 2.995$ Å (obtained from our CP2K PBE calculations of bulk rutile, see SI Secion S1 for details). Graphene was represented with an orthorhombic unit cell for ease of fitting with rutile (110) (see Figure 1), with the lattice parameters defined from the experimental value of the graphene carbon-carbon bond length (1.42 Å).
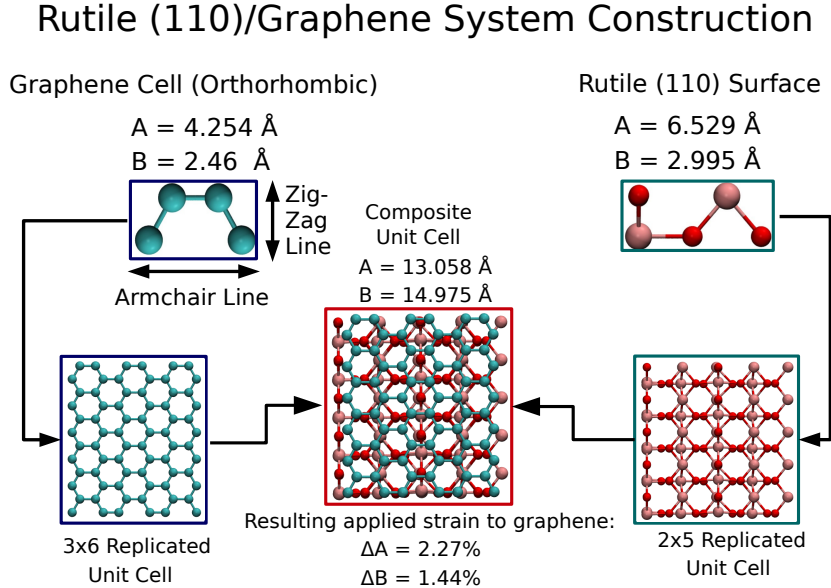

Figure 1: Construction of the composite rutile (110)/graphene unit cell used in this research

It was found that the best compromise of system size with commensurability was to fit a 3×6 (armchair × zigzag) supercell of graphene with a 2×5 supercell of rutile (110), where the armchair line of graphene runs parallel to the **A** lattice vector of rutile (110) (Figure 1). This composite UC results in an applied strain to graphene of +2.27% and +1.44% in the armchair and zigzag lines, respectively. This is the same size of the composite unit cell as

9

was used a previous DFT+U study of the rutile (110)-graphene interface.[41] This smallest commensurate unit cell, if used with a thin 6 atomic layer rutile (110) slab (two unit-cell layers), has a total of 192 atoms (40 TiO_2 units and 72 carbon atoms); the 9 atomic layer (three unit-cell layers) rutile (110) slab results in a 252-atom cell; both were used in this work.

An alternative UC of the composite was also considered, where the zigzag line of graphene runs parallel to the **A** cell vector of rutile (110). Here the smallest identified commensurate unit cell ("commensurate" defined here as having mismatch under 5%) comprised of an 8×5 supercell of graphene with a 3×7 supercell of rutile (110), this resulted in an applied compressive strain of -1.43% and -0.47% to the armchair and zigzag graphene directions, respectively. This composite UC, containing a total of 412 atoms with a 6 atomic layer slab of rutile (110), was constructed to investigate the effect of orientation of graphene relative to rutile (110) on the physical properties of the interface. The structure (interfacial C-O distances) and interfacial interaction energies (described in the next section) were very similar to the smaller cell described above and in Figure 1, therefore this larger cell was not investigated further.

Larger composite unit cells with smaller lattice mismatch can be constructed (see SI Section S1: Tables S1-S6 and Figure S1 for details), but their cell sizes become too large for practical use, and improvements in quality are expected to be minimal.

Results and Discussion

Effects of Lattice Strain on Graphene

The fact that the two crystal systems are non-commensurate leads to lattice mismatch and applied compressive or tensile strain at the interface. This issue is encountered *e.g.* in epitaxial films and interfaces,[91,92] which often have strong chemical bonding at the interfaces, and also in computational studies of any periodic composite system because of the need to

construct finite-size cells.[93] Due to the greater geometric flexibility of graphene relative to rutile, the final lattice parameters are chosen to fit the rutile (110) component, forcing graphene to be deformed. This may change the electronic properties of graphene in such interfaces, compared to isolated graphene. Thus far, computational studies of the TiO_2-graphene interfaces have not explored the structural and electronic effects that this applied strain may have on the graphene component of the system.

The effect of strain was, however, explored in fundamental studies of pristine graphene. While some studies indicated that an applied tensile deformation of 1% to the graphene lattice was sufficient to introduce a band gap,[86,94] further investigations[87-89,95-97] instead showed that the observed band gap opening in graphene was due to the migration of the Dirac point (where the band structure of graphene moves from insulating to metallic) from its original position at the high symmetry **k**-point 'K', as a direct consequence of the change in lattice symmetry. It was found that the applied deformation required to introduce a band gap in graphene is at least 26.5% for uniaxial tensile strain (only in the zigzag direction);[95,96] the gap can also be opened by anisotropic biaxial strain combining tension (11% in the zigzag direction) and compression (-20% in the armchair direction).[89] Notably, these levels of strain are quite close to the predicted[98,99] and measured[100] failure strain of graphene, $20 - 25\%$. While these levels of strain are much higher than those encountered in our composite cell, we will set out to explore the effect of low levels of strain on the electronic properties of graphene.

In this work lattice deformation was applied to the orthorhombic graphene cell in the zigzag and armchair directions, up to ± 6 % strain in steps of 1% relative to the fully optimised cell. In addition, much larger strain values of up to $\pm 30\%$ (*i.e.* up to the predicted strains for gap opening[95,96] and for graphene's mechanical failure[98-100]) in steps of 5% were also tested to determine the strain required to open a band gap in graphene. The fundamental band gaps (Figure 2 and Table S7) were obtained based on the band structures produced for each of the unstrained and strained cells (see examples in Figure 3 and in Figure S2 in
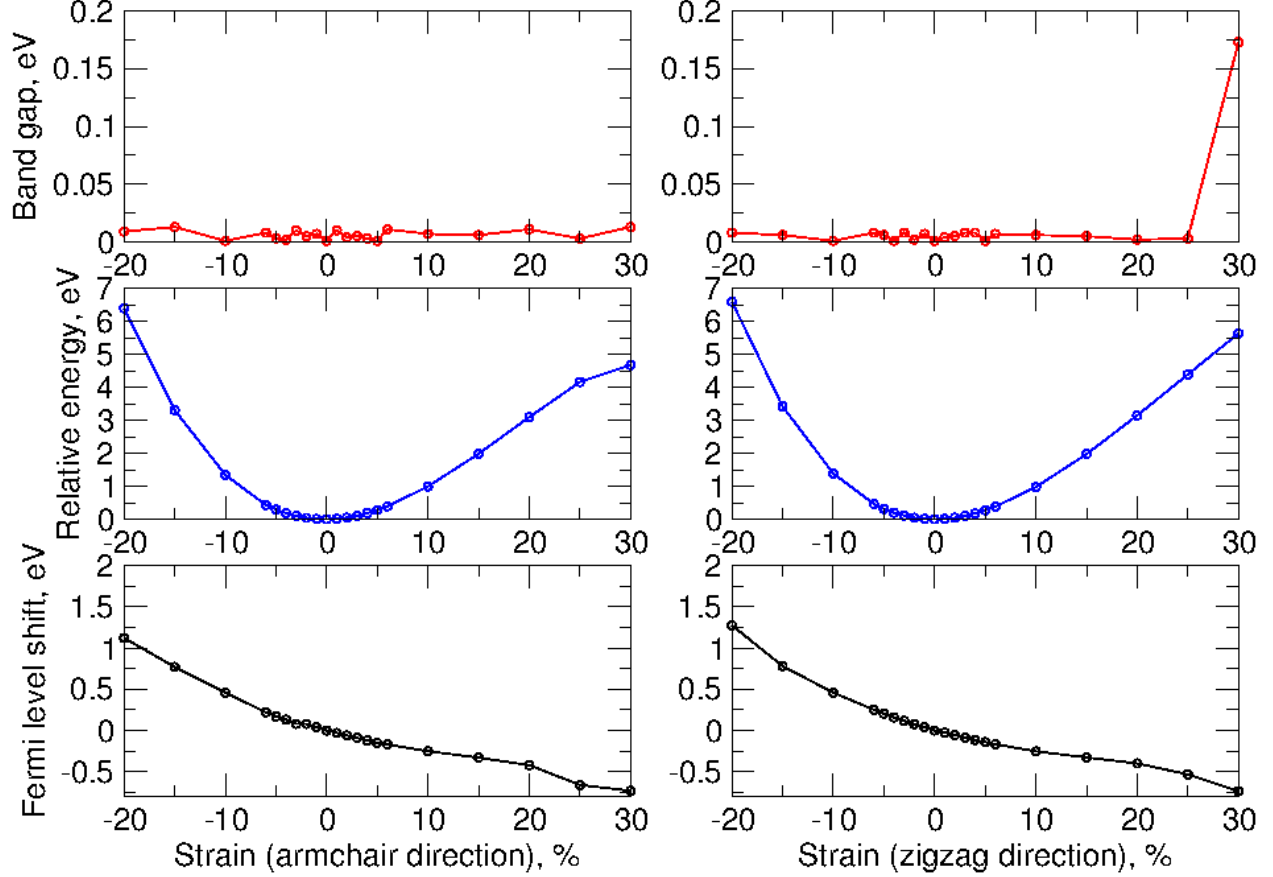
11

Figure 2: Effect of strain on the physical properties of graphene. Top row: change in the calculated band gap; middle row: total energy relative to the fully optimised orthorhombic graphene, bottom row: shift of the Fermi level compared to the unstrained graphene. Left column: strain is applied along the armchair direction: right column: strain is applied along the zigzag direction.

the SI).

The band gap values show that the structure remains a conductor through most of the low values of strain tested. There is no significant change observed in the band structure for graphene under applied tensile or compressive uniaxial strain. The Dirac point remains observable up to $\pm 6\%$ applied strain (the amount of strain that we have assumed acceptable for commensurate cells) and as far as $-20\% - +25\%$ strain. Consequently, the observed fundamental band gaps show very little variation from zero (close to or below the accuracy limit of 0.01 eV caused by the finite k-point sampling, see SI Section S2 for details), nor any discernible pattern, for all applied strains between -20% and $+25\%$ in both uniaxial

12

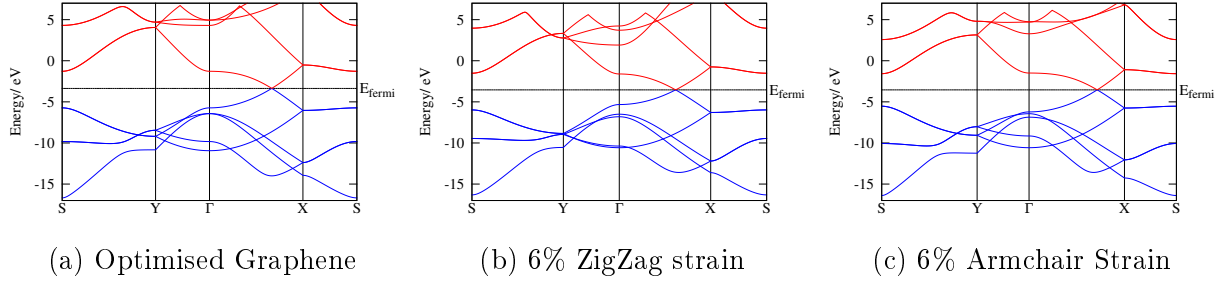| (a) Optimised Graphene | (b) 6% ZigZag strain | (c) 6% Armchair Strain |

Figure 3: Band structures of orthorhombic graphene cells: optimised (a), 6% zigzag tensile strain (b), and 6% armchair tensile strain (c). Occupied bands are represented in blue, unoccupied bands are in red, and the dashed line represents the Fermi level. Slight changes in the band shapes and a migration of the Dirac point along the Γ-X line can be seen.

directions. Only at the highest tested level of strain, 30% stretching in the zigzag direction, the Dirac point disappears and a band gap can be observed, which agrees with literature observations.[89,95,96]

As an additional test of accuracy of our graphene electronic structure, the Fermi velocity v_F was calculated for the unstrained and +6% stretched (armchair and zigzag direction) graphene: the v_F values were 1.54×10^6 m s^{-1}, 1.57×10^6 m s^{-1} and 1.30×10^6 m s^{-1}, respectively. These values are in good agreement with the experimentally measured range $(1.15 - 2.49) \times 10^6$ m s^{-1} (where the variation depends on the substrate where graphene was deposited)[101] and with theoretical values: $(0.85 - 0.9) \times 10^6$ m s^{-1} (LDA calculations)[101,102] and $(1.0 - 1.25) \times 10^6$ m s^{-1} (GW calculations);[102] the trend in our values of v_F is also in good agreement with recent calculations[103] which reported a slight increase and a decrease upon stretching in the armchair and zigzag direction, respectively. These results give additional confirmation that our modelling of graphene band structure is reliable.

While there is no band gap opening in graphene observed at low levels of strain, there is however an increase in the total energy, which follows a roughly parabolic trend (Figure 2): very small changes (below 0.1 eV) for the first ±2% of applied strain and is relatively minor changes (below 0.5 eV) for the first ±6%, followed by a rapid increase. These changes in the total energy result in a shift of the energy levels and thus will result in a change in the work function of graphene in the composite: the change in the work function is small (within ±0.2

eV) for the first $\pm 6\%$ of applied strain, but becomes larger for hypothetical large applied strain (Figure 2 and Table S7). Any shift in band energies will therefore have a direct impact on where the valence band of graphene lies in relation to rutile (110), and at large strains it may affect the predicted transfer of charge across the interface.

In conclusion, we have demonstrated that the small applied strain on the graphene component in our composite system will not disrupt the semimetallic properties of graphene in the system, nor will it have a significant effect on its band positions.

Binding Properties of the TiO$_2$/Graphene Interface

To investigate the physical properties of the TiO$_2$/graphene composite system, the interlayer spacing, and interface interaction energies and binding energies were calculated using CP2K with the PBE + D method. For this work the interlayer spacing is determined as the vertical (z-axis) distance, in Ångströms, between the uppermost atomic layer of two-coordinated oxygen atoms of rutile (110) and the graphene layer. The interface interaction energy is defined as:

$$E_{int} = E_{tot} - E_{ru-opt} - E_{gr-opt} + E_{BSSE} \tag{1}$$

where E_{int} is the interaction energy, E_{tot} is the computed total energy of the system, E_{ru-opt} is the total energy of the optimised rutile (110) slab, E_{gr-opt} is the total energy of the optimised graphene sheet, and E_{BSSE} is the basis set superposition error correction. The interaction energy can be decomposed into the *deformation* energy E_{def} (the energy change when deforming the TiO$_2$ and graphene components upon formation of the composite structure) and the *binding* energy E_{bind} (the energy gain due to the binding of these deformed components, or, the interaction energy excluding the change due to deformation) defined as:

$$E_{bind} = E_{int} - E_{def} \tag{2}$$

$$E_{def} = (E_{ru-def} - E_{ru-opt}) + (E_{gr-def} - E_{gr-opt}) \qquad (3)$$

where E_{ru-def} and E_{gr-def} are, respectively, the energies of the rutile (110) and graphene components in the geometry of the composite system. Interaction and binding energies and interlayer spacing for our system and a few reference systems are provided in Table S8. The interaction energies calculated in this work (-0.019 to -0.023 eV per carbon atom and -1.35 to -1.67 eV per cell) are very similar to the literature values for the same rutile (110)-graphene interface obtained using a different method (LDA+U).[41] These weak interaction energies indicate physisorption. Dispersion is the principal mechanism of the interaction, *e.g.* in the system with the 9-layer TiO_2 slab, dispersion contributes -3.13 eV to the binding energy of -3.24 eV. The alternative orientation of graphene above rutile, where the zigzag line of graphene is parallel to the **A** cell vector of rutile (110), results in very similar energies per carbon atom, confirming that interaction energies are very weakly dependent on the interfacial orientation, as expected for physisorption. Therefore the selected orientation of graphene above TiO_2 is representative of the properties of the many possible random orientations which may occur in experimental TiO_2/graphene composites.

Comparing our interface interaction energies (scaled per carbon atom) to the literature values for the anatase (101)-graphene interface (-0.032 to -0.050 eV per carbon atom),[44,50] the rutile (110)-based system is less strongly bound, probably because fewer atoms in the rutile (110) surface are close enough to graphene (only 2-coordinated surface oxygens). Comparing the rutile (110)/graphene composite to graphite, the composite's interaction energies per carbon atom are half as small as computational and experimental values for the interlayer binding in graphite and multilayer graphene[104,105] — this can be expected, since the TiO_2-graphene interface does not offer π-stacking such as found in graphite.

The deformation energies are 1.03 and 1.56 eV for the 6- and 9-atomic-layer TiO_2 slabs, respectively. A large part of this is the deformation of graphene resulting mainly from the lattice mismatch (see the computational methods section). This gives an energy change due

to deformation of 0.68 and 0.83 eV/cell for the 3 and 2-layer composite systems respectively. The deformation of rutile (110) costs 0.22 and 0.89 eV in the 6- and 9-atomic-layer TiO2 slabs, respectively.

The difference between the 6-layer and 9-layer TiO_2 systems is related to the well-known oscillation of physical properties in odd- and even-layer rutile (110) slabs: for example, odd-layer rutile (110) slabs are found to have higher surface energies than even-layer slabs.[79–82] The results of this work are in agreement with this pattern: since the 9-layer slab has a larger surface energy, it displays a larger energy gain due to the formation of the interface with graphene, especially obvious in the binding energies which do not include deformation.
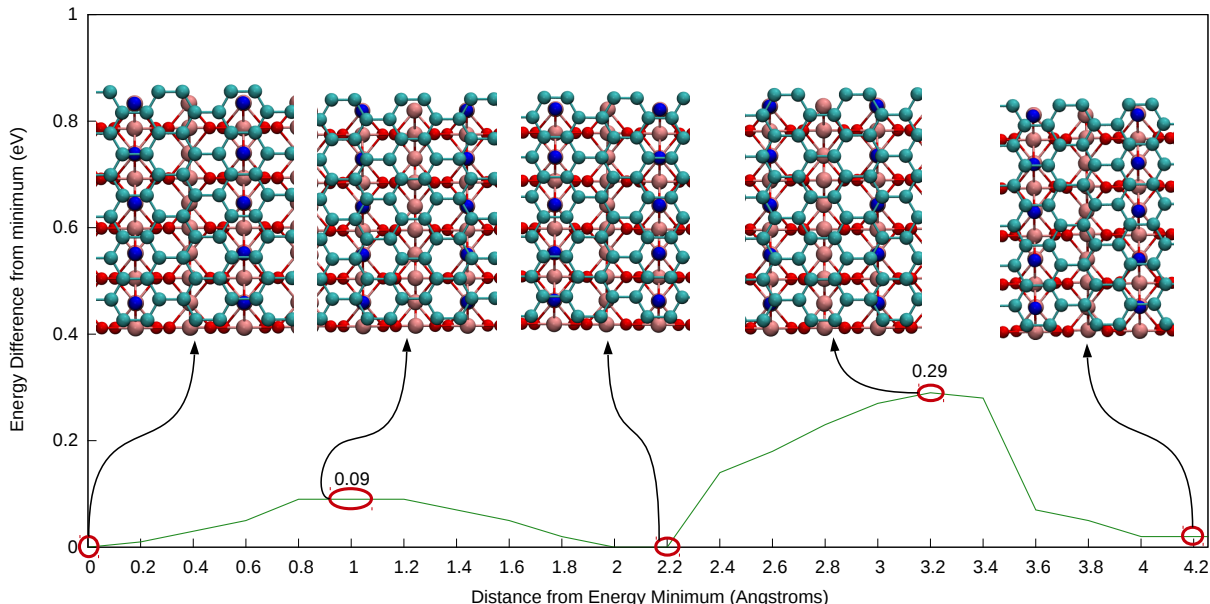

Figure 4: One-dimensional potential energy surface (PES) plot of the rutile (110)/graphene composite. Insets show the alignment of graphene carbon atoms (teal) with the surface 2-coordinated oxygen atoms (blue) at several positions (maxima and minima) of the PES.

To study the effect of the alignment of graphene above the rutile (110) surface, the potential energy surface (PES) was sampled by moving the graphene sheet in both the A and B directions of the composite unit cell (defined in Figure 1), initially in steps of 0.6 Å in both directions and then additionally in steps of 0.2 Å in the A direction. The analysis showed very little variation in energy (0.03 eV) upon displacement along the B direction

(graphene moving along the row of 2-coordinated oxygens of TiO_2), while the displacement along the A direction showed noticeable changes in energy. It can be seen in Figure 4 that the total energy increases as the carbon atoms in the graphene layer approach the 2-coordinated oxygen atoms in the rutile (110) surface layer, and is the most favourable when C–C bonds in the graphene layer rest over the top of these surface oxygen atoms (see insets in Figure 4). The energies vary by up to only 0.29 eV/cell. This very small variation suggests that there is no strongly preferred position of graphene above rutile (110). Diffusion along the B direction is essentially barrierless (0.03 eV) at room temperature. In the A direction, it is also easy to overcome the small barrier of 0.09 eV; the highest barrier of 0.29 eV results in the rate of approximately one movement every 10 ns (estimated using the Arrhenius equation with the prefactor of 10^{13} s^{-1}). Therefore, a variety of graphene/TiO_2 positions and orientations are likely to exist in experimental systems. Note, however, that this conclusion is true only for defect-free graphene; once oxygen functional groups are introduced to create graphene oxide, diffusion is likely to be impeded.

In conclusion, we have demonstrated that the interface between rutile (110) and graphene forms through a physisorption interaction, slightly weaker than the strength of interaction in multilayer graphene. The potential energy surface for this system is largely flat in shape, however, there exists a weak preference for aligning the surface 2-coordinated oxygen atoms with the mid-point of the carbon–carbon bonds in the graphene layer above.

Electronic Properties of the Rutile (110)/Graphene Interface

To analyse the posibility of charge transfer in the rutile (110)/graphene interface, we investigated the alignment of the electronic energy levels of TiO_2 and graphene in the composite system. Projected density of states (PDoS) spectra for the 6- and 9-atomic-layer rutile (110)/graphene composites and their corresponding isolated rutile (110) slabs have been calculated using the HSE06 hybrid functional in CRYSTAL14 (see Figure 5 and Figure S3 in the SI; all DoS plots incorporate vacuum level correction, as stated in the Computational
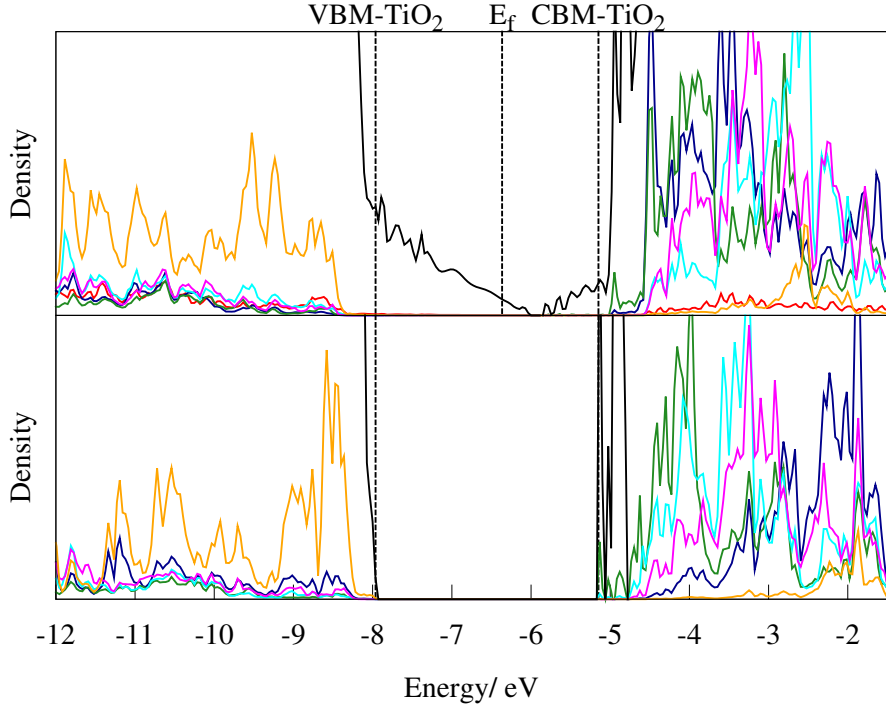
Methods section).

Figure 5: PDoS spectra of the 9 atomic layer rutile (110) slab (bottom) and its composite with graphene (top). The projections shown are: carbon (red), surface site 5-coordinated titanium (dark blue), surface site 6-coordinated titanium (cyan), subsurface titanium positions: below surface Ti_{5c} (green); below surface Ti_{6C} (purple), 2-coordinated oxygen (orange). The total DoS is shown in black. The dashed lines represent the valence and conduction bands of the isolated rutile (110) slab and the Fermi-level of the composite.

The band gaps of isolated TiO_2 slabs are found to be 3.9 eV in the 6-layer system and 2.8 eV in the 9-layer system (band edges are shown with dashed lines in Figure 5 and Figure S3). This variation in the band gap values reflects the odd-even slabs' oscillation of properties, characteristic of rutile (110): the band gaps are notably larger than the bulk value for even-layer slabs and smaller for odd-layer slabs.[79–82] Overall, the band gaps found in this work are in good agreement with the value of 3.39 eV found for bulk rutile with the same HSE06 functional in Ref.[63] and with the experimental values of 3.0 eV for the optical gap[106] and 3.3 ± 0.5 eV fundamental band gap[107] for rutile.

The graphs Figure 5 and Figure S3 show that both in isolated TiO_2 and in the composite

system the conduction band (CB) is primarily made up of titanium states, and the valence band (VB) of oxygen states, as is known from the literature on TiO_2 bulk and surfaces.[80,81] In the 6 atomic layer rutile (110) systems the conduction band contains both the 5-coordinated Ti (Ti_{5c}) and 6-coordinated Ti (Ti_{6c}) surface states in roughly equal intensities (Figure S3). In the composite system containing the 9 atomic layer rutile (110) slab, the states localised on 5-coordinated titanium atoms and subsurface titanium atoms immediately below dominate in the low-energy part of the CB. The most prominent difference between the isolated rutile (110) slab and the composite is the shift of the surface 5-coordinated titanium atoms' states (dark blue line in Figure 5) towards the low-energy part of the CB of the composite, which confirms electronic interaction between the TiO_2 surface and graphene.
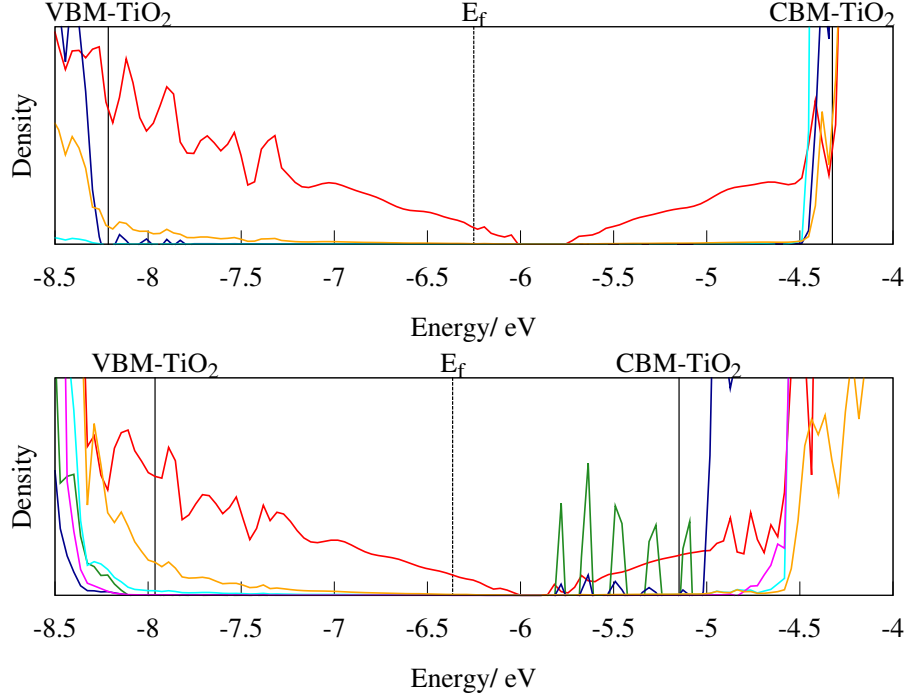

Figure 6: PDoS spectra of the 6 (top) and 9 (bottom) atomic layer rutile (110)/graphene composites. The projections shown are: Carbon (red), 5-coordinated titanium (dark blue), 6-coordinated titanium (cyan), subsurface titanium (green: below 5-coordinated surface site, purple: below 6-coordinated surface site), and 2-coordinated oxygen (orange). The dashed line represents the Fermi level, the solid black lines represent the valence and conduction band edges of the isolated rutile (110) slab.

The high-resolution PDoS plots in Figure 6 show that both the upper part of the valence

19

band and the lowest part of the conduction band of the composite system (both located in the TiO_2 band gap region) are made up mostly of graphene states. Notably, the graphene-dominated conduction band edge is ~ 0.8 eV and ~ 1.3 eV, in composites with the 9- and 6-atomic-layer rutile (110) slabs respectively, below the Ti-dominated high-intensity states of the conduction band (which start between -5.0 and -4.5 eV). We observe that the unoccupied states of graphene lie well below the unoccupied states of TiO_2 which is in agreement with experimental work function and electron affinity values, which show graphene to have a larger work function (measured as 4.5 eV[108] or between 4.89 and 5.16 eV,[109]) compared to TiO_2 (work function of rutile (110) experimentally measured as 4.2 eV;[110] electron affinity experimentally measured as $4.3 - 4.4$ eV[111,112] and calculated as 4.7 eV[112]).

Note that this alignment of Ti and carbon states is different from several recently published studies of TiO_2-graphene interfaces, where the graphene conduction band edge as usually found to lie near, just below, or just above the TiO_2 band edge.[41,44,47,49,50] There is, however, no agreement on the alignment of C- and Ti-based conduction band states in the published studies, and there are examples of C states being lower in energy than Ti states, similar to the results of this work, notably in graphene interfaces with anatase (001)[45,48] and rutile (110).[46] This difference is likely to be caused by differences in the electronic properties of anatase and rutile polymorphs of TiO_2 (indeed, the CB of anatase is believed to be $0.2 - 0.4$ eV below that of rutile[113,114]). It is also likely that the TiO_2 band positions in the DFT+U calculations[41,44–46,48] are affected by the choice of the 'U' parameter which is applied to describe the on-site Coulomb interaction of Ti 3d electrons. We believe that hybrid functionals offer a less ambiguous description of band gaps and band positions. In particular, the HSE06 functional used in this work accurately predicts the band gaps, band positions and defect states in TiO_2.[63,113,115] This functional has also been successfully used to describe optical properties of carbon nanotubes,[116] band gaps of carbon nanoribbons[117] and workfunctions of graphene, carbon nanoribbons and nanotubes.[118,119] With this good description of the individual TiO_2 and nanocarbon components, it can be expected that this

20

functional's description of the TiO_2-graphene interface is also reliable.

This position of graphene-dominated states far below TiO_2 states rather than just below TiO_2 states has important implications for charge transfer in this composite system: it is strongly favourable for photoexcited electrons to decay to the bottom of the conduction band, *i.e.* to these low-lying graphene-dominated states.

The high-resolution PDoS plots (Figure 6) show a clear qualitative difference between the composite systems involving 9-atomic-layer and 6-atomic layer TiO_2 slabs. In the 6-layer-based composite, only carbon-based states appear in the band gap of TiO_2, suggesting very little electronic interaction between graphene and TiO_2. By contrast, in the 9-layer-based composite, Ti-based states appear together with the carbon-based states near the bottom of the conduction band, in what would be the TiO_2 band gap. This points to electronic interaction between carbon and TiO_2 components, as these states are not present in the rutile component alone (see Figure 5). This mixture of titanium and carbon states in the conduction band is likely to affect the nature of charge transfer in this system. To investigate the origin of these Ti states, we plot the band structure and then explore the atomic orbitals which make up these bands.

The band structure of the 9 atomic layer composite is compared to the corresponding DoS spectrum in Figure 7. The band structure clearly shows that the Dirac point of graphene is preserved and can be seen close to the Γ point, along the $\Gamma-Y$ line. The Fermi level lies slightly below the Dirac point, indicating hole doping of graphene; this is confirmed by the electron density difference plot (Figure S4 in the SI), which shows some electron transfer from graphene to TiO_2. The amount of charge transferred has been evaluated as 0.68 electrons per cell (or 0.01 electrons per carbon atom), which is comparable to 0.02 electrons per carbon found for the similar system in Ref.[41] The downshift of the Fermi level (0.42 eV) is slightly smaller than in the previously reported study of this interface using the DFT + U method (0.65 eV[41]). Comparing the band structure of the composite system in Figure 7 with the band structure of the isolated rutile slab and isolated graphene sheet (Figure S5), we can see
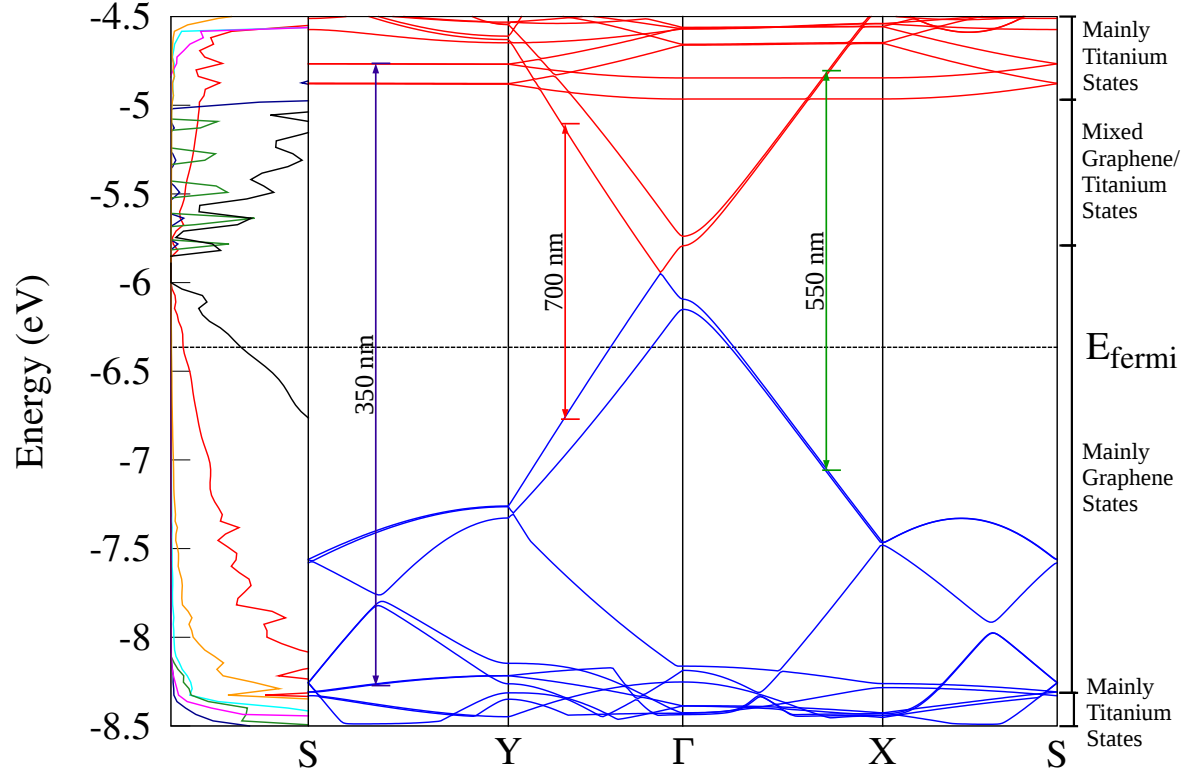
Figure 7: Band structure of the 9 atomic layer rutile (110)/graphene composite system, showing 10 occupied bands (shown in blue) and 10 unoccupied bands (in red). The PDoS spectrum of this interface is shown to the left, with the total DoS included in black, and guide-lines relating parts of the DoS spectrum to the band structure. Additional annotations show the energies of possible electronic transitions and the composition of various regions of the band structure (assigned according to the analysis shown in Figure 8)

that the electronic structure of TiO_2 and graphene remain essentially intact in the composite system. Although the Dirac point has not been captured in our DoS plots (Figure 6 and S3), it is clearly present in the band structure. The apparent band gap in the DoS, similar to the small[44,46,47] or very small[50] band gaps observed in some of the previous studies of TiO_2/graphene interfaces, has likely been caused by the use of insufficiently dense **k**-point grids, similar to the early studies of strained isolated graphene alone.[86,94] The absence of a band gap means that electrons can be easily promoted to the unoccupied graphene states. From these spectra it can also be seen that the thermodynamically favoured location of photoexcited electrons will be on graphene.

The question still remains about the origin of Ti-based states in the region corresponding to the band gap of pure TiO_2. These states do not correspond to any special points in the conduction band (see Figure 7). The DoS plots in Figure 6 show that these states are localised on subsurface (bulk-like) Ti atoms of the 9 atomic layer rutile slab. The 6 atomic layer slab, which has no bulk-like Ti atoms, has no such gap states. This shows that subsurface Ti atoms are essential for strong electronic interaction between TiO_2 and graphene and that the 6 atomic layer slab, which has no subsurface atoms, is too small to model the rutile-graphene interface. The narrower band gap of the odd-layer rutile slab also brings the conduction band edge closer to the highest occupied band of graphene, facilitating the electronic interaction between graphene and TiO_2 (in agreement with the larger binding energy of graphene with the 9 atomic layer rutile slab). The localisation on subsurface Ti atoms is in qualitative agreement with the LDA+U study of Du *et al.*,[41] which showed that the first two CB states are predominantly based on graphene and subsurface Ti atoms below surface Ti_{5c}. This important role of the subsurface Ti atoms in the TiO_2 rutile (110)/graphene interaction is likely related to the tendency of excess electrons in rutile (110) slabs to localise at subsurface Ti sites.[120,121] Since there is some charge transfer from graphene to TiO_2 in the ground state (as shown above), these subsurface Ti atoms are the most likely sites to accommodate this excess charge, and thus the presence of even one subsurface layer enhances the rutile (110)/graphene interlayer binding.

From these results one can see that, in order to correctly model the properties of this composite system, at least one subsurface layer of rutile (110) must be present. Thus the 9-layer rutile (110) slab is the smallest slab sufficient to describe this system, and we expect that thicker rutile (110) slabs will behave qualitatively similar.

To understand the origin of the Ti-based gap states, eigenvalues (atomic orbital (AO) coefficients) of several highest occupied and lowest unoccupied bands were analysed. Squares (complex conjugates) of AO coefficients $c_{i,j,k}c^*_{i,j,k}$ (where i is the atom number, j is the orbital (eigenstate), k is the **k**-point) were calculated and summed over all Ti, all O and all C atoms,

to give the contributions of Ti, O and C to each eigenstate at each **k**-point: $\sum cc^*_{Ti,j,k}$, $\sum cc^*_{O,j,k}$ and $\sum cc^*_{C,j,k}$. The analysis of the AO coefficients at the **k**-points along the band structure path (Figure 8) confirms that the highest occupied band (labelled "VBM") as a whole consists mainly of carbon states. Similarly, the 3 highest energy VBs consist entirely of carbon states, and titanium and oxygen states begin to emerge at the VBM-4 and lower (energy -8.3 eV and below in Figure 7). The lowest unoccupied band (labelled "CBM") around the Γ-point, and along most of the Γ-X and Γ-Y lines, consists mainly of carbon states, while at and around **k**-points X, Y, and S it is predominantly titanium. These rutile titanium bands can be identified easily by their characteristically flat profiles – they are essentially the same as lowest-energy unoccupied bands of isolated rutile (also seen as intense peaks in the DoS, starting at ~ -5.0 eV, see Figure 5 and Figure 6).

The band lines in Figure 7 and Figure 8 look smooth and do not reflect the sharp Ti peaks seen near the bottom of the CB in the DoS. However, the band structure is plotted along special high-symmetry lines in the Brillouin zone (BZ), while the DoS is calculated by integrating over the whole BZ. To explain the DoS shape, we analysed atomic orbital coefficients of the highest occupied and two lowest unoccupied states across the full BZ. The contributions by atom type ($\sum c^c*_{Ti,j,k}$, $\sum cc^*_{O,j,k}$ and $\sum cc^*_{C,j,k}$) were calculated for VBM, CBM and CBM+1 on the $12 \times 12 \times 1$ grid of **k**-points covering the whole BZ (the same grid as used in the DOS calculations).

Figure 9 shows these AO contributions for the CBM and CBM+1, plotted on a 2D grid covering the irreducible part of the BZ of the composite. The sizes of circles in Figure 9 correspond to the magnitude of the species' contribution to each of these bands at each **k**-point. The VBM (results not shown) is predominantly $(97 - 99\%)$ composed of C states at all considered **k**-points, in agreement with our DoS and band line analysis. The CBM is separated into two regions. Across most of the BZ (from -6.0 to -5.0 eV), this band is entirely localised on carbon atoms with negligible contributions from Ti and O atoms; however, the regions of the BZ immediately next to the X-S and Y-S lines (at > -5.0 eV) are
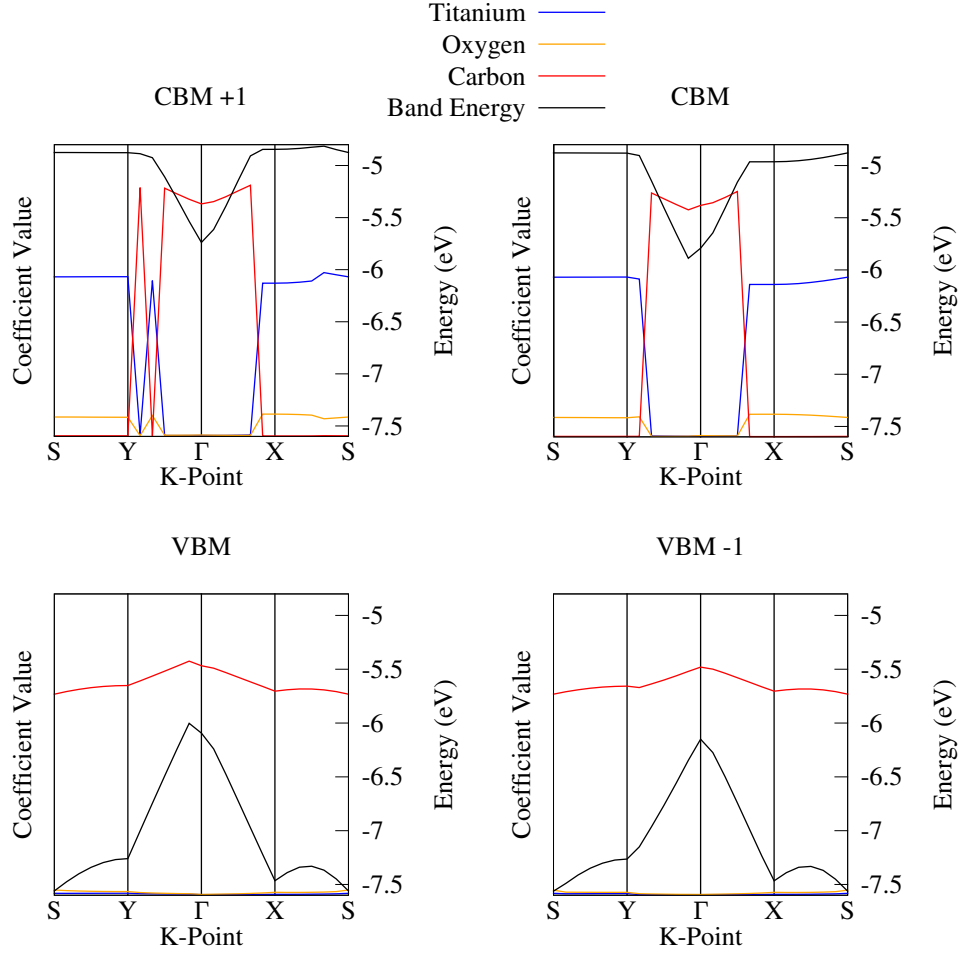
Figure 8: Energies of selected bands (VBM-1, VBM, CBM, CBM+1), plotted together with the sums of squared atomic orbital coefficients for all titanium, oxygen, and carbon species in the 9 atomic layer composite system. These data points cover all **k**-points in the path chosen for the band structure in Figure 7

almost entirely localised on Ti atoms with very small contributions of O atoms. The second unoccupied band (labelled "CBM+1") has the most interesting pattern of atomic orbitals' contributions across the BZ: the regions next to the X-S and Y-S lines are again almost entirely localised on Ti atoms, the region around the Γ point is entirely localised on C atoms, while in the intermediate BZ region, as the electron energies increase, the main contributors change from C to Ti. Thus, Ti contributions appear at lower energies than in pure TiO_2. Therefore, this second unoccupied band is not entirely graphitic and demonstrates electronic interaction between the carbon and TiO_2 components of the composite. Interestingly, there
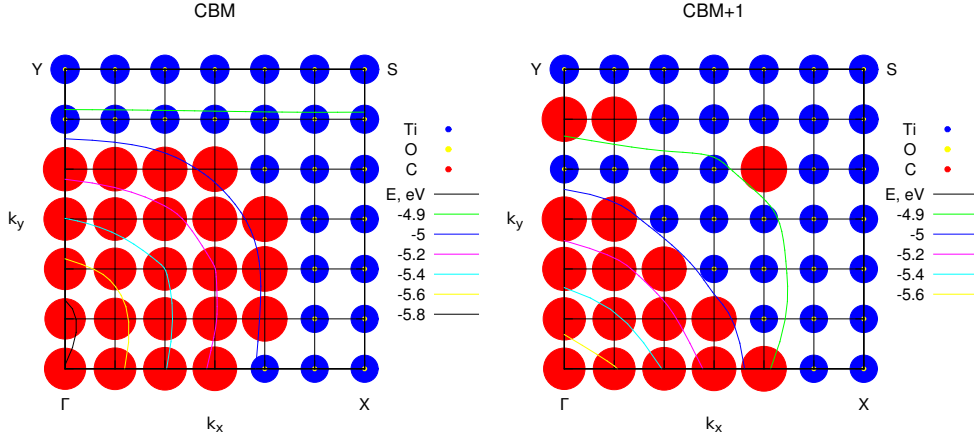
25

Figure 9: Sums of squared atomic orbital coefficients (shown as circles) for all titanium, oxygen, and carbon species in the 9 atomic layer composite system, plotted in the irreducible part of the Brillouin zone of the rutile (110)/graphene composite system. The areas of the circles correlate with the magnitude of each atomic species' contribution to the eigenstate (CBM or CBM+1) at each k-point (blue circles for Ti, yellow for O, red for C). The variation of these bands' energies across the BZ is shown with thin contour lines.

are no "mixed" states equally made up of C and Ti at any of the points in the BZ in this region; there is clear separation between C-dominated and Ti-dominated states.

Applying this analysis of atomic orbitals to the DoS plot in Figure 6 and Figure 7, it becomes clear that the carbon contributions in the low-energy region of the CB (-6.0 to -5.0 eV) come from both the first and the second unoccupied bands, while the titanium contributions come only from the second unoccupied band, at certain points in the BZ. The observation that Ti states contribute at some rather than all points in the BZ explains why the Ti states appear as spikes rather than as a smooth band in the DoS. This appearance of Ti states alongside C states in the graphene-like lower part of the CB is an indication of electronic interaction between graphene and rutile (110) - notably, interaction with subsurface (bulk-like) Ti atoms.

From this analysis of the electronic structure, and from the evidence in published research,[38,39,41] it is now possible to infer more details about the mechanism of photosensitisation enhancement upon irradiation of this composite system. The combination of our DoS,

26

band structure, and atomic orbital coefficient analysis enable us to make predictions about the likely nature of photoexcitation transitions in the TiO_2-graphene system. We note that a calculation of transition dipole moments and electronic excitations would be necessary for a full description of photoexcitation processes. This is beyond the scope of the current work, however, a qualitative picture of photoexcitation can be obtained from our DoS and atomic orbital data. Our data suggest that the mechanism of photoexcitation will differ depending on the energy of a given incident photon. For a visible-region photon (2.5–1.5 eV, some possible transitions shown schematically by red and green arrows in Figure 7), electronic transitions must originate from a carbon state within graphene. The excited state reached by the transition may then be either carbon- or titanium-based depending upon the photon energy. Very low-energy photons can excite only carbon π to π^* electronic transitions (*i.e.* no charge transfer). Visible-light photons can span the band gap further away from the Γ point and nearer the points X and Y, where titanium states begin to appear in the unoccupied states. Then, these titanium states may accept the photoexcited electron, resulting in graphene $\rightarrow$ TiO_2 transition (although the intensity of this transition is likely to be lower than that of the graphene $\rightarrow$ graphene transition, because the charge transfer excitation has smaller transition matrix elements due to small overlap of the wavefunction).

Thus, the experimentally observed broadening of the absorption range of the TiO_2 composites[22,24,30,32–37] is attributed to the presence of these mixed graphene and titanium states. Transfer of photoinduced electrons to TiO_2 creates an efficient photoreduction catalyst.[16,20] Note however, that the lowest-energy unoccupied states are all graphene-based (both at the bottom of the conduction band and just above the Fermi level), therefore the thermodynamically favourable process is for the photoexcited electrons to eventually decay to these lowest-energy unoccupied carbon states. Thus, photoexcited charge transfer from graphene to TiO_2 is likely to be only a transient phenomenon (cf. a recent experimental study[122] highlights the complex nature of recombination of hot electrons injected from graphene to TiO_2), unless photoexcited electrons and holes rapidly diffuse in TiO_2 or are used elsewhere,

for example, in photocatalytic reactions. Similarly, if an electron is supplied from elsewhere (e.g. using molecular sensitisers[123]), it will most likely end up in these graphene-based lowest-occupied carbon states. Both processes make graphene the electron-rich part of the composite, so that it may act as an electron shuttle in complex photocatalyst architectures, as proposed by Kamat.[40] It is also those electrons in the lowest-energy unoccupied carbon states which are then likely to recombine with holes in the valence band.

Photons in the ultraviolet range (> 3.0 eV) are able to excite transitions that originate from deeper levels in the lower VBs, which are localised on TiO_2. The accepting states are likely to be mixed graphene/titanium or purely titanium based, thus the overall direction of the charge transfer in this case is from TiO_2 to graphene, as observed in many UV-Vis experiments.[38,42]

In all cases that we have discussed, the final states reached by photoexcitations are likely to involve both carbon- and titanium-based states. The direct carbon π to π^* electronic excitations are likely to be more intense than charge-transfer carbon$\rightarrow TiO_2$ excitations[39,41] even if the energy of the excitation is the same. These carbon π to π^* excitations, however, can be followed by excited-state charge injection to same-energy titanium-based states, as observed by Manga et al[42] and described computationally by Long et $al.$[43] Experimental data showing the visible-region photon absorption enhancement provided by graphene in this system[38,39] support this model of a combination of direct (e.g. carbon $\pi - \pi^*$) and charge-transfer excitations.

Conclusions

In summary, we have performed a quantum chemical study with the aim to model the rutile (110)/graphene composite photocatalyst system, using 6 and 9 atomic layer rutile (110) slabs. The potential inaccuracy associated with the mismatch in lattice parameters between the rutile and graphene components in the system has been evaluated. Here it is shown that

small compressive and tensile strain on graphene from the mismatch results in only small increase in total energy and negligible opening of the band gap (up to 0.01 eV) in the case of mismatches of 6% or fewer, and shows that the lattice mismatch of our chosen system (1.4-2.3 %) is small enough to have no effect on the electronic properties of graphene. The interfacial interaction and binding energies have been calculated for both 6 and 9 atomic layer composites, which show that the interaction strength is noticeably greater for the 9 atomic layer system than the 6-atomic layer system. For the 9 atomic layer system specifically, the calculated interaction energy per carbon atom (-0.045 eV/atom) is comparable to that of graphite.[104]

Separation of photoinduced charges is one of the most beneficial properties of TiO_2-graphene composte photocatalysts: thanks to this separation of charges, electron-hole recombination is greatly reduced, resulting in long-lived electrons and holes. We inverstigate the nature of charge separation in this composite by analysing the density of states, band structure and orbital composition of this material. We show that the lowest unoccupied states of these composites are dominated by graphene, therefore after relaxation (but before decaying to the valence band) photoexcited electrons are likely to end up in the graphene component. Our analysis of the electronic structure of the TiO_2-graphene composites elucidates how different wavelengths of photons are likely to result in different types of photoinduced charge separation. For example, visible light photons are likely to induce electron excitations from entirely carbon-based states (top of the VB) to both C- and Ti-based states (overall photoinduced electron transfer graphene $\rightarrow$ TiO_2), while UV photons may produce excitations from Ti-based states (deeper in the VB) again to both C- and Ti-based states (overall photoinduced electron transfer $TiO_2\rightarrow$graphene). Thus, photoexcitations with the different charge-transfer characters are possible, depending on the excitation wavelength. However, both types of photoexcitations produce charge-transfer states, thus creating electron-rich and hole-rich materials for photocatalytic reduction and oxidation.

The use of a hybrid DFT functional has demonstrated that correcting the unphysical

self-interaction energy present in pure DFT functionals is important for the accurate simulation of this composite's electronic properties. The application of modern computational techniques and supercomputing resources in this research has shown that hybrid HF/DFT level calculations are possible on a large system such as this interface.

Finally, it should be noted that this work focussed entirely on composites formed by pristine graphene. As many experimental systems are synthesised from graphene oxide,[29] the realistic composite may contain a number of oxygen functional groups, such as epoxy, hydroxyl and carboxyl,[33] which may form bridges between graphene and titanium dioxide and have been suggested as an important contributor to electron transfer between TiO_2 and graphene.[47,50,60] Therefore one of our future directions will be to investigate the difference between pristine graphene and graphene oxide in terms of the composition of occupied and unoccupied bands and the direction of charge transfer.

Supporting Information Available

The following files are available free of charge. Construction of commensurate unit cells; strain testing data; additional band structures of strained graphene; interaction energy data; density of states spectra; charge density difference images; band structures of isolated TiO_2 and graphene; an example of the input file used for the 9-atomic layer rutile (110)/graphene composite system.

Acknowledgement

Notes

The authors declare no competing financial interest

References

(1) Highfield, J. Advances and Recent Trends in Heterogeneous Photo(Electro)-Catalysis for Solar Fuels and Chemicals. *Molecules* **2015**, *20*, 6739–6793.

(2) Etacheri, V.; Di Valentin, C.; Schneider, J.; Bahnemann, D.; Pillai, S. C. Visible-Light Activation of TiO_2 Photocatalysts: Advances in Theory and Experiments. *J. Photochem. Photobiol. C* **2015**, *25*, 1–29.

(3) Maeda, K. Z-Scheme Water Splitting Using Two Different Semiconductor Photocatalysts. *ACS Catal.* **2013**, *3*, 1486–1503.

(4) Teoh, W. Y.; Scott, J. A.; Amal, R. Progress in Heterogeneous Photocatalysis: From Classical Radical Chemistry to Engineering Nanomaterials and Solar Reactors. *J. Phys. Chem. Lett.* **2012**, *3*, 629–639.

(5) Chen, X.; Shen, S.; Guo, L.; Mao, S. S. Semiconductor-based Photocatalytic Hydrogen Generation. *Chem. Rev.* **2010**, *110*, 6503–6570.

(6) Kudo, A.; Miseki, Y. Heterogeneous Photocatalyst Materials for Water Splitting. *Chem. Soc. Rev.* **2009**, *38*, 253–278.

(7) Fujishima, A.; Honda, K. Electrochemical Photolysis of Water at a Semiconductor Electrode. *Nature* **1972**, *238*, 37–38.

(8) Liu, Z.; Bai, H.; Sun, D. Facile Fabrication of Hierarchical Porous TiO_2 Hollow Microspheres with High Photocatalytic Activity for Water Purification. *Appl. Catal. B* **2011**, *104*, 234–238.

(9) Wang, B.; Li, C.; Cui, H.; Zhang, J.; Zhai, J.; Li, Q. Shifting Mechanisms in the Initial Stage of Dye Photodegradation by Hollow TiO_2 Nanospheres. *J. Mat. Sci.* **2013**, *49*, 1336–1344.

(10) Lee, S. S.; Bai, H.; Liu, Z.; Sun, D. D. Novel-Structured Electrospun TiO_2/CuO Composite Nanofibers for High Efficient Photocatalytic Cogeneration of Clean Water and Energy from Dye Wastewater. *Water research* **2013**, *47*, 4059–4073.

(11) Song, H.; Chen, T.; Sun, Y.-l.; Zhang, X.-Q.; Jia, X.-h. Controlled Synthesis of Porous Flower-Like TiO_2 Nanostructure with Enhanced Photocatalytic Activity. *Ceramics International* **2014**, *40*, 11015–11022.

(12) Yang, R.; Yang, L.; Tao, T.; Ma, F.; Xu, M.; Zhang, Z. Contrastive Study of Structure and Photocatalytic Performance with Three-Dimensionally Ordered Macroporous CuO-TiO_2 and CuO/TiO_2. *Appl. Surf. Sci.* **2014**, *288*, 363–368.

(13) Zhang, N.; Yang, M.-Q.; Liu, S.; Sun, Y.; Xu, Y.-J. Waltzing with the Versatile Platform of Graphene to Synthesize Composite Photocatalysts. *Chem. Rev.* **2015**, *115*, 10307–10377.

(14) Kapilashrami, M.; Zhang, Y.; Liu, Y.-S.; Hagfeldt, A.; Guo, J. Probing the Optical Property and Electronic Structure of TiO_2 Nanomaterials for Renewable Energy Applications. *Chem. Rev.* **2014**, *114*, 9662–9707.

(15) Dahl, M.; Liu, Y.; Yin, Y. Composite Titanium Dioxide Nanomaterials. *Chem. Rev.* **2014**, *114*, 9853–9889.

(16) Reddy, K. R.; Hassan, M.; Gomes, V. G. Hybrid Nanostructures based on Titanium Dioxide for Enhanced Photocatalysis. *Appl. Catal. A* **2015**, *489*, 1–16.

(17) Li, J.; Wu, N. Semiconductor-based Photocatalysts and Photoelectrochemical Cells for Solar Fuel Generation: a Review. *Catal. Sci. Technol.* **2015**, *5*, 1360–1384.

(18) Kumar, S. G.; Devi, L. G. Review on Modified TiO_2 Photocatalysis under UV/Visible Light: Selected Results and Related Mechanisms on Interfacial Charge Carrier Transfer Dynamics. *J. Phys. Chem. A* **2011**, *115*, 13211–13241.

(19) Pinaud, B. A.; Benck, J. D.; Seitz, L. C.; Forman, A. J.; Chen, Z.; Deutsch, T. G.; James, B. D.; Baum, K. N.; Baum, G. N.; Ardo, S. et al. Technical and Economic Feasibility of Centralized Facilities for Solar Hydrogen Production via Photocatalysis and Photoelectrochemistry. *Ener. & Env. Sci* **2013**, *6*, 1983–2002.

(20) Xiang, Q.; Yu, J.; Jaroniec, M. Graphene-based Semiconductor Photocatalysts. *Chem. Soc. Rev.* **2012**, *41*, 782–796.

(21) Leary, R.; Westwood, A. Carbonaceous Nanomaterials for the Enhancement of TiO_2 Photocatalysis. *Carbon* **2011**, *49*, 741–772.

(22) Khan, G.; Choi, S. K.; Kim, S.; Lim, S. K.; Jang, J. S.; Park, H. Carbon Nanotubes as an Auxiliary Catalyst in Heterojunction Photocatalysis for Solar Hydrogen. *Appl. Catal. B* **2013**, *142-143*, 647–653.

(23) Zhang, J.; Zhu, Z.; Tang, Y.; Feng, X. Graphene encapsulated hollow TiO_2 nanospheres: efficient synthesis and enhanced photocatalytic activity. *Journal of Materials Chemistry A* **2013**, *1*, 3752–3756.

(24) Cargnello, M.; Grzelczak, M.; Rodríguez-González, B.; Syrgiannis, Z.; Bakhmutsky, K.; La Parola, V.; Liz-Marzán, L. M.; Gorte, R. J.; Prato, M.; Fornasiero, P.

Multiwalled Carbon Nanotubes Drive the Activity of Metal@Oxide Core-Shell Catalysts in Modular Nanocomposites. *J. Am. Chem. Soc.* **2012**, *134*, 11760–6.

(25) Woan, K.; Pyrgiotakis, G.; Sigmund, W. Photocatalytic Carbon-Nanotube-TiO_2 Composites. *Adv. Mat.* **2009**, *21*, 2233–2239.

(26) Jitianu, A.; Cacciaguerra, T.; Benoit, R.; Delpeux, S.; Béguin, F.; Bonnamy, S. Synthesis and Characterization of Carbon Nanotubes-TiO_2 Nanocomposites. *Carbon* **2004**, *42*, 1147–1151.

(27) Vincent, P.; Brioude, A.; Journet, C.; Rabaste, S.; Purcell, S.; Le Brusq, J.; Plenet, J. Inclusion of Carbon Nanotubes in a TiO_2 Sol-Gel Matrix. *J. Non-Cryst. Solids* **2002**, *311*, 130–137.

(28) Iijima, S. Helical Microtubules of Graphitic Carbon. *Nature* **1991**, *354*, 56–58.

(29) Williams, G.; Seger, B.; Kamat, P. V. TiO_2-Graphene Nanocomposites. UV-Assisted Photocatalytic Reduction of Graphene Oxide. *ACS Nano* **2008**, *2*, 1487–1491.

(30) Shao, P.; Tian, J.; Shi, W.; Gao, S.; Cui, F. Eco-Friendly One-Pot Synthesis of Ultradispersed TiO_2 Nanocrystals/Graphene Nanocomposites with High Photocatalytic Activity for Dye Degradation. *J. Mater. Chem. A* **2015**, *3*, 19913–19919.

(31) Yang, M. Q.; Xu, Y. J. Basic Principles for Observing the Photosensitizer Role of Graphene in the Graphene-Semiconductor Composite Photocatalyst from a Case Study on Graphene-ZnO. *J. Phys. Chem. C* **2013**, *117*, 21724–21734.

(32) Sha, J.; Zhao, N.; Liu, E.; Shi, C.; He, C.; Li, J. In Situ Synthesis of Ultrathin 2-D TiO_2 with High Energy Facets on Graphene Oxide for Enhancing Photocatalytic Activity. *Carbon* **2014**, *68*, 352–359.

(33) Pastrana-Martínez, L. M.; Morales-Torres, S.; Likodimos, V.; Falaras, P.; Figueiredo, J. L.; Faria, J. L.; Silva, A. M. T. Role of Oxygen Functionalities on

the Synthesis of Photocatalytically Active Graphene-TiO$_2$ Composites. *Appl. Catal. B* **2014**, *158-159*, 329–340.

(34) Yang, M.-Q.; Zhang, N.; Xu, Y.-J. Synthesis of Fullerene-, Carbon Nanotube-, and Graphene-TiO$_2$ Nanocomposite Photocatalysts for Selective Oxidation: A Comparative Study. *ACS Appl. Mat. & Interfaces* **2013**, *5*, 1156–1164.

(35) Perera, S. D.; Mariano, R. G.; Vu, K.; Nour, N.; Seitz, O.; Chabal, Y.; Balkus, K. J. Hydrothermal Synthesis of Graphene-TiO$_2$ Nanotube Composites with Enhanced Photocatalytic Activity. *ACS Catal.* **2012**, *2*, 949–956.

(36) Fan, W.; Lai, Q.; Zhang, Q.; Wang, Y. Nanocomposites of TiO$_2$ and Reduced Graphene Oxide as Efficient Photocatalysts for Hydrogen Evolution. *J. Phys. Chem. C* **2011**, *115*, 10694–10701.

(37) Zhang, H.; Lv, X.; Li, Y.; Wang, Y.; Li, J. P25-Graphene Composite as a High Performance Photocatalyst. *ACS Nano* **2010**, *4*, 380–386.

(38) Pastrana-Martínez, L. M.; Morales-Torres, S.; Likodimos, V.; Figueiredo, J. L.; Faria, J. L.; Falaras, P.; Silva, A. M. T. Advanced Nanostructured Photocatalysts based on Reduced Graphene Oxide-TiO$_2$ Composites for Degradation of Diphenhydramine Pharmaceutical and Methyl Orange Dye. *Appl. Catal. B* **2012**, *123-124*, 241–256.

(39) Liang, Y. T.; Vijayan, B. K.; Lyandres, O.; Gray, K. A.; Hersam, M. C. Effect of Dimensionality on the Photocatalytic Behavior of Carbon-Titania Nanosheet Composites: Charge Transfer at Nanomaterial Interfaces. *J. Phys. Chem. Lett.* **2012**, *3*, 1760–1765.

(40) Kamat, P. V. Graphene-Based Nanoarchitectures. Anchoring Semiconductor and Metal Nanoparticles on a Two-Dimensional Carbon Support. *J. Chem. Phys. Lett.* **2010**, *1*, 520–527.

(41) Du, A.; Ng, Y. H.; Bell, N. J.; Zhu, Z.; Amal, R.; Smith, S. C. Hybrid Graphene/Titania Nanocomposite: Interface Charge Transfer, Hole Doping, and Sensitization for Visible Light Response. *J. Phys. Chem. Lett.* **2011**, *2*, 894–899.

(42) Manga, K. K.; Zhou, Y.; Yan, Y.; Loh, K. P. Multilayer Hybrid Films Consisting of Alternating Graphene and Titania Nanosheets with Ultrafast Electron Transfer and Photoconversion Properties. *Adv. Func. Mater.* **2009**, *19*, 3638–3643.

(43) Long, R.; English, N. J.; Prezhdo, O. V. Photo-Induced Charge Separation across the Graphene-TiO_2 Interface Is Faster than Energy Losses: A Time-Domain ab Initio Analysis. *J. Am. Chem. Soc.* **2012**, *134*, 14238–14248.

(44) Li, X.; Gao, H.; Liu, G. A LDA+U Study of the Hybrid Graphene/Anatase TiO_2 Nanocomposites: Interfacial Properties and Visible Light Response. *Comp. Theor. Chem.* **2013**, *1025*, 30–34.

(45) Masuda, Y.; Giorgi, G.; Yamashita, K. DFT Study of Anatase-Derived TiO_2 Nanosheets/Graphene Hybrid Materials. *Phys. Stat. Solidi B* **2014**, *251*, 1471–1479.

(46) Zhou, C.; Zhao, X. Effects of Interfacial Structure and Polarity on Charge Transfer Between Carbonaceous Nanomaterials and Rutile (110) Surface. *Comp. Mater. Sci.* **2013**, *69*, 180–185.

(47) Yang, N.; Liu, Y.; Wen, H.; Tang, Z.; Zhao, H.; Li, Y.; Wang, D. Photocatalytic Properties of Graphdiyne and Graphene Modified TiO_2: From Theory to Experiment. *ACS Nano* **2013**, *7*, 1504–1512.

(48) Gao, H.; Li, X.; Lv, J.; Liu, G. Interfacial Charge Transfer and Enhanced Photocatalytic Mechanisms for the Hybrid Graphene/Anatase TiO_2(001) Nanocomposites. *J. Phys. Chem. C* **2013**, *117*, 16022–16027.

(49) Qian, W.; Greaney, P. A.; Fowler, S.; Chiu, S.-K.; Goforth, A. M.; Jiao, J. Low-Temperature Nitrogen Doping in Ammonia Solution for Production of N-Doped TiO_2-Hybridized Graphene as a Highly Efficient Photocatalyst for Water Treatment. *ACS Sustainable Chem. Eng.* **2014**, *2*, 1802–1810.

(50) Ferrighi, L.; Fazio, G.; Di Valentin, C. Charge Carriers Separation at the Graphene/(101) Anatase TiO_2 Interface. *Adv. Mat. Int.* **2016**, *3*, 1500624.

(51) Xu, L.; Huang, W.-Q.; Wang, L.-L.; Huang, G.-F. Interfacial Interactions of Semiconductor with Graphene and Reduced Graphene Oxide: CeO_2 as a Case Study. *ACS Appl. Mat. Interfaces* **2014**, *6*, 20350–20357.

(52) Yang, Y.-C.; Xu, L.; Huang, W.-Q.; Luo, C.-Y.; Huang, G.-F.; Peng, P. Electronic Structures and Photocatalytic Responses of $SrTiO_3$ (100) Surface Interfaced with Graphene, Reduced Graphene Oxide, and Graphane: Surface Termination Effect. *J. Phys. Chem. C* **2015**, *119*, 19095–19104.

(53) Geng, W.; Liu, H.; Yao, X. Enhanced photocatalytic properties of titania-graphene nanocomposites: a density functional theory study. *Phys. Chem. Chem. Phys.* **2013**, *15*, 6025–6033.

(54) Ayissi, S.; Charpentier, P. A.; Farhangi, N.; Wood, J. A.; Palotas, K.; Hofer, W. A. Interaction of Titanium Oxide Nanostructures with Graphene and Functionalized Graphene Nanoribbons: A DFT Study. *J. Phys. Chem. C* **2013**, *117*, 25424–25432.

(55) Favaro, M.; Agnoli, S.; Di Valentin, C.; Mattevi, C.; Cattelan, M.; Artiglia, L.; Magnano, E.; Bondino, F.; Nappini, S.; Granozzi, G. TiO_2/Graphene Nanocomposites from the Direct Reduction of Graphene Oxide by Metal Evaporation. *Carbon* **2014**, *68*, 319–329.

(56) Bukowski, B.; Deskins, N. A. The Interactions Between TiO_2 and Graphene with

Surface Inhomogeneity Determined using Density Functional Theory. *Phys. Chem. Chem. Phys.* **2015**, *17*, 29734–29746.

(57) Fischer, J. M. T. A.; Hankel, M.; Searles, D. J. Computational Studies of the Interaction of Carbon Dioxide with Graphene-Supported Titanium Dioxide. *J. Phys. Chem. C* **2015**, *119*, 29044–29051.

(58) Gao, H.; Lu, B.; Li, D.; Guo, F.; Dai, D.; Si, C.; Liu, G.; Zhao, X. Photoactivity and Electronic Properties of Graphene-like Materials and TiO_2 Composites using First-Principles Calculations. *RSC Adv.* **2016**, *6*, 65315–65321.

(59) Umrao, S.; Abraham, S.; Theil, F.; Pandey, S.; Ciobota, V.; Shukla, P. K.; Rupp, C. J.; Chakraborty, S.; Ahuja, R.; Popp, J. et al. A Possible Mechanism for the Emergence of an Additional Band Gap due to a Ti-O-C Bond in the TiO_2-Graphene Hybrid System for Enhanced Photodegradation of Methylene Blue under Visible Light. *RSC Adv.* **2014**, *4*, 59890–59901.

(60) Long, R. Understanding the Electronic Structures of Graphene Quantum Dot Physisorption and Chemisorption onto the TiO_2 (110) Surface: A First-Principles Calculation. *ChemPhysChem* **2013**, *14*, 579–582.

(61) Jia, C.; Ma, W.; Gu, C.; Chen, H.; Yu, H.; Li, X.; Zhang, F.; Gu, L.; Xia, A.; Hou, X. et al. High-Efficiency Selective Electron Tunnelling in a Heterostructure Photovoltaic Diode. *Nano Lett.* **2016**, *16*, 3600–3606.

(62) Liu, S.; Guo, E.; Yin, L. Tailored visible-light driven anatase TiO_2 photocatalysts based on controllable metal ion doping and ordered mesoporous structure. *J. Mater. Chem.* **2012**, *22*, 5031–5041.

(63) Landmann, M.; Rauls, E.; Schmidt, W. G. The Electronic Structure and Optical Response of Rutile, Anatase and Brookite TiO_2. *J. Phys.: Condens. Matter* **2012**, *24*, 195503.

38

(64) Di Valentin, C.; Pacchioni, G.; Selloni, A. Electronic Structure of Defect States in Hydroxylated and Reduced Rutile TiO_2 Surfaces. *Phys. Rev. Lett.* **2006**, *97*, 166803.

(65) Anisimov, V. I.; Zaanen, J.; Andersen, O. K. Band theory and Mott insulators: Hubbard U instead of Stoner I. *Phys. Rev. B* **1991**, *44*, 943–954.

(66) Li, W.; Walther, C. F. J.; Kuc, A.; Heine, T. Density Functional Theory and Beyond for Band-Gap Screening: Performance for Transition-Metal Oxides and Dichalcogenides. *J. Chem. Theory Comput.* **2013**, *9*, 2950–2958.

(67) Janotti, A.; Van de Walle, C. G. LDA + U and Hybrid Functional Calculations for Defects in ZnO, SnO_2, and TiO_2. *Phys. Status Solidi B* **2011**, *248*, 799–804.

(68) Marsman, M.; Paier, J.; Stroppa, A.; Kresse, G. Hybrid Functionals Applied to Extended Systems. *J. Phys.: Condens. Matter* **2008**, *20*, 064201.

(69) Ferrighi, L.; Datteo, M.; Fazio, G.; Di Valentin, C. Catalysis under Cover: Enhanced Reactivity at the Interface between (Doped) Graphene and Anatase TiO_2. *J. Am. Chem. Soc.* **2016**, *138*, 7365–7376.

(70) Heyd, J.; Scuseria, G. E.; Ernzerhof, M. Hybrid Functionals Based on a Screened Coulomb Potential. *J. Chem. Phys.* **2003**, *118*, 8207–8215.

(71) Heyd, J.; Scuseria, G. E.; Ernzerhof, M. Erratum: "Hybrid Functionals Based on a Screened Coulomb Potential". *J. Chem. Phys.* **2006**, *124*, 219906.

(72) Janotti, A.; Varley, J. B.; Rinke, P.; Umezawa, N.; Kresse, G.; Van de Walle, C. G. Hybrid Functional Studies of the Oxygen Vacancy in TiO_2. *Phys. Rev. B* **2010**, *81*, 085212.

(73) Vandevondele, J.; Krack, M.; Mohamed, F.; Parrinello, M.; Chassaing, T.; Hutter, J. Quickstep: Fast and Accurate Density Functional Calculations Using a Mixed Gaussian and Plane Waves Approach. *Comput. Phys. Commun.* **2005**, *167*, 103–128.

(74) Dovesi, R.; Orlando, R.; Erba, A.; Zicovich-Wilson, C. M.; Civalleri, B.; Casassa, S.; Maschio, L.; Ferrabone, M.; De La Pierre, M.; D'Arco, P. et al. CRYSTAL14 : A Program for the Ab Initio Investigation of Crystalline Solids. *Int. J. Quantum Chem.* **2014**, *114*, 1287–1317.

(75) Perdew, J. P.; Burke, K.; Ernzerhof, M. Generalized Gradient Approximation Made Simple. *Phys. Rev. Lett.* **1996**, *77*, 3865–3868.

(76) Grimme, S. Semiempirical GGA-Type Density Functional Constructed with a Long-Range Dispersion Correction. *J. Comput. Chem.* **2006**, *27*, 1787–1799.

(77) Goedecker, S.; Teter, M.; Hutter, J. Separable Dual-space Gaussian Pseudopotentials. *Phys. Rev. B* **1996**, *54*, 1703–1710.

(78) VandeVondele, J.; Hutter, J. Gaussian Basis Sets for Accurate Calculations on Molecular Systems in Gas and Condensed Phases. *J. Chem. Phys.* **2007**, *127*, 114105.

(79) Bates, S.; Kresse, G.; Gillan, M. A Systematic Study of the Surface Energetics and Structure of TiO_2 (110) by First-Principles Calculations. *Surf. Sci.* **1997**, *385*, 386–394.

(80) Bredow, T.; Giordano, L.; Cinquini, F.; Pacchioni, G. Electronic Properties of Rutile TiO_2 Ultrathin Films: Odd-Even Oscillations with the Number of Layers. *Phys. Rev. B* **2004**, *70*, 35419.

(81) Labat, F.; Baranek, P.; Adamo, C. Structural and Electronic Properties of Selected Rutile and Anatase TiO_2 Surfaces: An ab Initio Investigation. *J. Chem. Theory Comput.* **2008**, *4*, 341–352.

(82) Martsinovich, N.; Jones, D. R.; Troisi, A. Electronic Structure of TiO_2 Surfaces and Effect of Molecular Adsorbates using Different DFT Implementations. *J. Phys. Chem. C* **2010**, *114*, 22659–22670.

(83) Kowalski, P. M.; Meyer, B.; Marx, D. Composition, Structure, and Stability of the Rutile $TiO_2(110)$ Surface: Oxygen Depletion, Hydroxylation, Hydrogen Migration, and Water Adsorption. *Phys. Rev. B* **2009**, *79*, 115410.

(84) Boys, S.; Bernardi, F. The Calculation of Small Molecular Interactions by the Differences of Separate Total Energies. Some Procedures with Reduced Errors. *Mol. Phys.* **1970**, *19*, 553–566.

(85) Guidon, M.; Hutter, J.; Vandevondele, J. Auxiliary Density Matrix Methods for Hartree-Fock Exchange Calculations. *J. Chem. Theory Comput.* **2010**, *6*, 2348–2364.

(86) Gui, G.; Li, J.; Zhong, J. Band Structure Engineering of Graphene by Strain: First-Principles Calculations. *Phys. Rev. B* **2008**, *78*, 075435.

(87) Gui, G.; Li, J.; Zhong, J. Reply to "Comment on 'Band Structure Engineering of Graphene by Strain: First-Principles Calculations'". *Physical Review B* **2009**, *80*, 167402.

(88) Naumov, I. I.; Bratkovsky, A. M. Gap Opening in Graphene by Simple Periodic Inhomogeneous Strain. *Phys. Rev. B* **2011**, *84*, 245444.

(89) Kerszberg, N.; Suryanarayana, P. Ab Initio Strain Engineering of Graphene: Opening Bandgaps up to 1 eV. *RSC Adv.* **2015**, *5*, 43810–43814.

(90) Peintinger, M. F.; Oliveira, D. V.; Bredow, T. Consistent Gaussian Basis Sets of Triple-Zeta Valence with Polarization Quality for Solid-State Calculations. *J. Comput. Chem.* **2013**, *34*, 451–459.

(91) Wolf, D. In *Materials Interfaces: Atomic-Level Structure and Properties*, 1st ed.; Wolf, D., Yip, S., Eds.; Chapman & Hall: London, 1992; Chapter 1, pp 1–57.

(92) Morgan, B. J. In *Computational Modeling of Inorganic Nanomaterials*; Bromley, S. T., Zwijnenburg, M. A., Eds.; CRC Press: Boca Raton, 2016; Chapter 3, pp 83–112.

(93) Van de Walle, C. G.; Martin, R. M. Theoretical calculations of heterojunction discontinuities in the Si/Ge system. *Phys. Rev. B* **1986**, *34*, 5621–5634.

(94) Ni, Z. H.; Yu, T.; Lu, Y. H.; Wang, Y. Y.; Feng, Y. P.; Shen, Z. X. Uniaxial Strain on Graphene: Raman Spectroscopy Study and Band-Gap Opening. *ACS Nano* **2008**, *2*, 2301–2305.

(95) Ni, Z. H.; Yu, T.; Lu, Y. H.; Wang, Y. Y.; Feng, Y. P.; Shen, Z. X. Uniaxial Strain on Graphene: Raman Spectroscopy Study and Band-Gap Opening. *ACS Nano* **2009**, *3*, 483–483.

(96) Pereira, V. M.; Castro Neto, A. H.; Peres, N. M. R. Tight-Binding Approach to Uniaxial Strain in Graphene. *Phys. Rev. B* **2009**, *80*, 045401.

(97) Cocco, G.; Cadelano, E.; Colombo, L. Gap Opening in Graphene by Shear Strain. *Phys. Rev. B* **2010**, *81*, 241412.

(98) Cadelano, E.; Palla, P. L.; Giordano, S.; Colombo, L. Nonlinear Elasticity of Monolayer Graphene. *Phys. Rev. Lett.* **2009**, *102*, 235502.

(99) Marianetti, C. A.; Yevick, H. G. Failure Mechanisms of Graphene under Tension. *Phys. Rev. Lett.* **2010**, *105*, 245502.

(100) Lee, C.; Wei, X.; Kysar, J. W.; Hone, J. Measurement of the Elastic Properties and Intrinsic Strength of Monolayer Graphene. *Science* **2008**, *321*, 385–388.

(101) Hwang, C.; Siegel, D. A.; Mo, S.-K.; Regan, W.; Ismach, A.; Zhang, Y.; Zettl, A.; Lanzara, A. Fermi Velocity Engineering in Graphene by Substrate Modification. *Sci. Rep.* **2012**, *2*, 590.

(102) Park, C.-H.; Giustino, F.; Spataru, C. D.; Cohen, M. L.; Louie, S. G. Angle-Resolved Photoemission Spectra of Graphene from First-Principles Calculations. *Nano Letters* **2009**, *9*, 4234–4239, PMID: 19856901.

(103) Wong, J.-H.; Wu, B.-R.; Lin, M.-F. Strain Effect on the Electronic Properties of Single Layer and Bilayer Graphene. *The Journal of Physical Chemistry C* **2012**, *116*, 8271–8277.

(104) Lebedeva, I. V.; Knizhnik, A. A.; Popov, A. M.; Lozovik, Y. E.; Potapkin, B. V. Interlayer Interaction and Relative Vibrations of Bilayer Graphene. *Phys. Chem. Chem. Phys.* **2011**, *13*, 5687–95.

(105) Benedict, L. X.; Chopra, N. G.; Cohen, M. L.; Zettl, A.; Louie, S. G.; Crespi, V. H. Microscopic Determination of the Interlayer Binding Energy in Graphite. *Chem. Phys. Lett.* **1998**, *286*, 490–496.

(106) Amtout, A.; Leonelli, R. Optical Properties of Rutile near Its Fundamental Band Gap. *Phys. Rev. B* **1995**, *51*, 6842–6851.

(107) Tezuka, Y.; Shin, S.; Ishii, T.; Ejima, T.; Suzuki, S.; Sato, S. Photoemission and Bremsstrahlung Isochromat Spectroscopy Studies of TiO_2 (Rutile) and $SrTiO_3$. *J. Phys. Soc. Jpn.* **1994**, *63*, 347–357.

(108) Lee, E. J. H.; Balasubramanian, K.; Weitz, R. T.; Burghard, M.; Kern, K. Contact and Edge Effects in Graphene Devices. *Nature Nanotechnology* **2008**, *3*, 486–490.

(109) Song, S. M.; Park, J. K.; Sul, O. J.; Cho, B. J. Determination of Work Function of Graphene under a Metal Electrode and its Role in Contact Resistance. *Nano Lett.* **2012**, *12*, 3887–3892.

(110) Imanishi, A.; Tsuji, E.; Nakato, Y. Dependence of the Work Function of TiO_2 (Rutile) on Crystal Faces, Studied by a Scanning Auger Microprobe. *J. Phys. Chem. C* **2007**, *111*, 2128–2132.

(111) Butler, M. A.; Ginley, D. S. Prediction of Flatband Potentials at SemiconductorâĂŘ-

Electrolyte Interfaces from Atomic Electronegativities. *Journal of The Electrochemical Society* **1978**, *125*, 228–232.

(112) Stevanovic, V.; Lany, S.; Ginley, D. S.; Tumas, W.; Zunger, A. Assessing Capability of Semiconductors to Split Water Using Ionization Potentials and Electron Affinities Only. *Phys. Chem. Chem. Phys.* **2014**, *16*, 3706–3714.

(113) Scanlon, D. O.; Dunnill, C. W.; Buckeridge, J.; Shevlin, S. A.; Logsdail, A. J.; Woodley, S. M.; Catlow, C. R. A.; Powell, M. J.; Palgrave, R. G.; Parkin, I. P. et al. Band Alignment of Rutile and Anatase TiO$_2$. *Nat. Mater.* **2013**, *12*, 798–801.

(114) Nosaka, Y.; Nosaka, A. Y. Reconsideration of Intrinsic Band Alignments within Anatase and Rutile TiO$_2$. *J. Phys. Chem. Lett.* **2016**, *7*, 431–434.

(115) Deák, P.; Aradi, B.; Frauenheim, T. Polaronic Effects in TiO$_2$ Calculated by the HSE06 Hybrid Functional: Dopant Passivation by Carrier Self-Trapping. *Phys. Rev. B* **2011**, *83*, 155207.

(116) Barone, V.; Peralta, J. E.; Scuseria, G. E. Optical Transitions in Metallic Single-Walled Carbon Nanotubes. *Nano Lett.* **2005**, *5*, 1830–1833.

(117) Barone, V.; Hod, O.; Scuseria, G. E. Electronic Structure and Stability of Semiconducting Graphene Nanoribbons. *Nano Lett.* **2006**, *6*, 2748–2754.

(118) Barone, V.; Peralta, J. E.; Uddin, J.; Scuseria, G. E. Screened Exchange Hybrid Density-Functional Study of the Work Function of Pristine and Doped Single-Walled Carbon Nanotubes. *J. Chem. Phys.* **2006**, *124*, 024709.

(119) Barone, V.; Hod, O.; Peralta, J. E.; Scuseria, G. E. Accurate Prediction of the Electronic Properties of Low-Dimensional Graphene Derivatives Using a Screened Hybrid Density Functional. *Acc. Chem. Res.* **2011**, *44*, 269–279.

(120) Deskins, N. A.; Rousseau, R.; Dupuis, M. Localized Electronic States from Surface Hydroxyls and Polarons in TiO$_2$(110). *The Journal of Physical Chemistry C* **2009**, *113*, 14583–14586.

(121) Maggio, E.; Martsinovich, N.; Troisi, A. Continuum and Atomistic Description of Excess Electrons in TiO$_2$. *Journal of Physics: Condensed Matter* **2016**, *28*, 074004.

(122) Williams, K. J.; Nelson, C. A.; Yan, X.; Li, L.-S.; Zhu, X. Hot Electron Injection from Graphene Quantum Dots to TiO$_2$. *ACS Nano* **2013**, *7*, 1388–1394.

(123) Lakadamyali, F.; Kato, M.; Reisner, E. Colloidal Metal Oxide Particles Loaded with Synthetic Catalysts for Solar H$_2$ Production. *Farad. Discuss.* **2012**, *155*, 191–205.

Graphical TOC Entry